TEKTONIKA

20th to 21st Century Relative Sea and Land Level Changes in Northern California: Tectonic Land Level Changes and their Contribution to Sea-Level Rise, Humboldt Bay Region, Northern California

Jason R. Patton *[1,2], **Todd B. Williams**[2], **Jeffrey K. Anderson**[3], **Mark Hemphill-Haley**[1], **Reed J. Burgette**[4], **Ray Weldon II**[5], **Robert C. McPherson**[1], **Thomas H. Leroy**[2,6]

[1]Cal Poly Humboldt, Department of Geology, 1 Harpst St., Arcata, CA 95521, USA | [2]Cascadia GeoSciences, 380 Beach Dr., Arcata, CA 95521, USA | [3]Northern Hydrology and Engineering, P.O. Box 2515, McKinleyville, CA 95519, USA | [4]Oregon Department of Geology and Mineral Industries, 800 NE Oregon Street, Suite 965, Portland, OR 97232, USA | [5]University of Oregon, Department of Earth Sciences, 1272 University of Oregon, Eugene, OR 97403 | [6]Pacific Watershed Associates, 1652 Holly Dr, McKinleyville, CA 95519, USA

Abstract Sea-level changes are modulated in coastal northern California by land-level changes due to the earthquake cycle along the Cascadia subduction zone, the San Andreas plate boundary fault system, and crustal faults. Sea-level rise (SLR) subjects ecological and anthropogenic infrastructure to increased vulnerability to changes in habitat and increased risk for physical damage. The degree to which each of these forcing factors drives this modulation is poorly resolved. We use NOAA tide gage data and 'campaign' tide gage deployments, Global Navigation Satellite System (GNSS) data, and National Geodetic Survey (NGS) first-order levelling data to calculate vertical land motion (VLM) rates in coastal northern California. Sea-level observations, highway level surveys, and GNSS data all confirm that land is subsiding in Humboldt Bay, in contrast to Crescent City where the land is rising. Subtracting absolute sea-level rate (∼1.99 mm/year) from Crescent City (CC) and North Spit (NS) gage relative sea-level rates reveals that CC is uplifting at ∼2.83 mm/year and NS is subsiding at ∼3.21mm/year. GNSS vertical deformation reveals similar rates of ∼2.60 mm/year of uplift at Crescent City. In coastal northern California, there is an E-W trending variation in vertical land motion that is primarily due to Cascadia megathrust fault seismogenic coupling. This interseismic subsidence also dominates the N-S variation in vertical land motion in most of the study region. There exists a second-order heterogeneous N-S trend in vertical land motion that we associate to crustal fault-related strain. There may be non-tectonic contributions to the observed VLM rates.

Executive Editor:
Robin Lacassin
Associate Editor:
Jack Williams
Technical Editor:
Mohamed Gouiza

Reviewers:
Raphael Grandin
Romain Jolivet

Submitted:
4 June 2022
Accepted:
12 December 2022
Published:
24 January 2023

1 Introduction

Since the Last Glacial Maximum (approximately 22 thousand years ago), global mean sea level (GMSL) has risen ∼120 meters (*Lambeck and Chappell*, 2001; *Peltier*, 2002; *Peltier and Fairbanks*, 2006). Present-day rise is attributed to natural and anthropogenic forcings contributing to melting ice, human management of surface and ground water, and changes in sea water temperature and salinity (*Cazenave and Llovel*, 2010). Following 1850, the anthropogenic forcing of Earth's climate has exerted a first order control to sea level rise (*Jevrejeva et al.*, 2009; *Stammer et al.*, 2013; *Church et al.*, 2013). As water and ice masses spatially redistribute, Earth's crust and mantle adjust to these changes; these elastic and viscoelastic isostatic adjustments further contribute to relative sea-level (RSL) with a process called the Glacial Isostatic Adjustment (GIA; *Peltier*, 1976; *Clark et al.*, 1978; *Gehrels*, 2010; *King et al.*, 2012).

For the period of 1925-2006, sea-level along the USA northwestern coast, from northern California to Washington state (herein after called Pacific Northwest), is estimated to be 2.28 ± 0.20 millimeters per year (mm/year; *Burgette et al.*, 2009). *Montillet et al.* (2018) present a northeast Pacific SLR rate of 1.99 ± 0.16 mm/year. Based on satellite altimetry, for the period of 1993-2007, global estimates of sea level rise range up to 3.4 ± 0.04 mm/year (*Cazenave and Llovel*, 2010; *Nerem et al.*, 2010). *He et al.* (2022) present a summary of geocentric satellite derived rates that range from 1.5 to 1.9 mm/year. However sea-level rise at the Humboldt Bay North Spit (NS) tide gage is much greater than any other gage in the Pacific Northwest (*Zervas*, 2009). National Oceanic and

*✉ Jason.Patton@humboldt.edu

Atmospheric Administration Center for Operational Oceanographic Products and Services (NOAA Co-Ops) reports an observed sea-level rate of 4.73 mm/year at the NS tide gage in Humboldt Bay (*Zervas et al.*, 2013). At the next nearest NOAA continuous operating tide gage in Crescent City (CC), California, sea-level is observed to be lowering at 0.65 mm/year (*Zervas et al.*, 2013), the result of upwards vertical land motion in Crescent City. The NS gage records led some previous researchers to discard these data as apparently anomalous (since they were not similar to the rates at CC), possibly due to localized site settlement (*Mitchell et al.*, 1994; *Verdonck*, 2006).

In 2010 we gathered over thirty federal, state, and local agencies, academics, non-governmental organizations, and private industry to discuss the factors that may control sea-level rise in coastal northern California. One focus was the difference in sense of motion for SLR rates between the North Spit and the Crescent City tide gages and we suggested to the workshop participants that this difference was due to the tectonics of the Cascadia subduction zone. The consensus from this workshop was that there was a need to evaluate the tectonic contribution to sea-level rise for coastal northern California.

After the 2010 workshop, others agreed with our interpretation that the high rate of sea-level rise at the North Spit tide gage was due to the tectonics related to the CSZ (*Komar et al.*, 2011). In this paper we address this question by analyzing GNSS, leveling, and other tide gage data.

When the NS tide gage was installed, 11 tidal benchmarks and associated temporary gaging stations were deployed from 1977 to 1980. Utilizing a subset of these initial observation points, we analyze contemporary sea-level observations in Humboldt Bay to investigate relative sea-level rise over local to regional scales. We also use first-order leveling data collected by the NGS to determine vertical land motion rates for the second half of the twentieth century (*Burgette et al.*, 2012). We also incorporate GNSS observations into our analyses of vertical land motion for the past two decades (*Murray and Svarc*, 2017).

The Gorda plate subducts beneath the North America plate at about 36 mm/year to form the Cascadia subduction zone (CSZ) megathrust fault (*McCaffrey et al.*, 2007, Figure 1). An excellent review of the horizontal GNSS data, which may help some learn about the horizontal plate tectonics, is presented in *McKenzie and Furlong* (2021) and included references. However, this convergence rate is limited to global plate circuit rate, locally controlled by magnetic anomalies observed in the Gorda and Juan de Fuca crust (*Wilson*, 2002). When the fault is seismogenically locked, the plate deforms elastically, causing vertical land motion (*Mitchell et al.*, 1994; *Flück et al.*, 1997; *Wang et al.*, 2003). Regions directly above the locked area of the fault generally subside during the interseismic period and regions landward of the locked region of the fault generally uplift during the interseismic period, as observed in Japan (*Hyndman and Wang*, 1995; *Loveless and Meade*, 2010) and elsewhere (*Wang et al.*, 2001; *Feng et al.*, 2012). The interseismic and coseismic VLM trends are dependent upon their relative timing within the earthquake cycle and the temporal extent to which the viscous mantle responds to the earthquake cycle, so coseismic motion may not be a perfect inversion of interseismic motion (*Wang and Tréhu*, 2016). The spatial variation in relative sea-level change, the sum of the vertical change based on sea-level rise and vertical land-level changes (*Nelson et al.*, 1996), has been used to quantify vertical tectonic deformation associated with the CSZ in Oregon (*Mitchell et al.*, 1994; *Burgette et al.*, 2009; *Zervas et al.*, 2013) and along the entire margin (*Verdonck*, 2006). Understanding this ongoing tectonic deformation in northern California will allow us to quantify and predict future sea-level trends. The North America plate crustal faults that may contribute to ongoing deformation in the Mendocino triple junction region are presented in Figure 2.

We utilize tide gage, benchmark releveling, and GNSS observations to characterize the interseismic plate tectonic land-level change associated with the southern CSZ (Figure 3). This paper includes a unified geodetic dataset for this region that uses three independent measures of vertical land motion. Results from this study will provide fundamental sea-level rise data for making management decisions as they apply to coastal landscapes and the species and ecosystems that inhabit the tidal prism, which are the most vulnerable to future sea-level rise (*Nicholls and Cazenave*, 2010; *Nicholls*, 2011). Quantifying future relative sea-level change is the first step in planning strategies for coastal ecosystems (*Church et al.*, 2011; *Horton et al.*, 2014). Preliminary results from this study were presented in a non-peer reviewed annual and final report to the U.S. Fish and Wildlife (*Patton et al.*, 2014, 2017) however results presented in this paper include additional efforts to account for updated SLR estimates (e.g., *Montillet et al.*, 2018; *He et al.*, 2022), VLM calculations, and updated GNSS rates.

2 Methods

We utilize water level observations in Humboldt Bay as collected by the NOAA (1977-1987), Towill Engineering on the behalf of the US Army Corps of Engineers San Francisco Office (2010), and Northern Hydrology and Engineering (2008, 2012-13, 2016) to evaluate local trends in sea level compared to Crescent City, the longest operating tide gage in the region (Figure 3). We use available first-order leveling data collected by the NGS predominantly along the route of Highway 101 between Crescent City south through and past the Humboldt Bay region (Figure 3). We also use GNSS observations from continuous GNSS sites operated by the National Science Foundation program, EarthScope, and the USGS (Figure 3). GNSS rate data are relative to the ITRF2014 reference frame. We

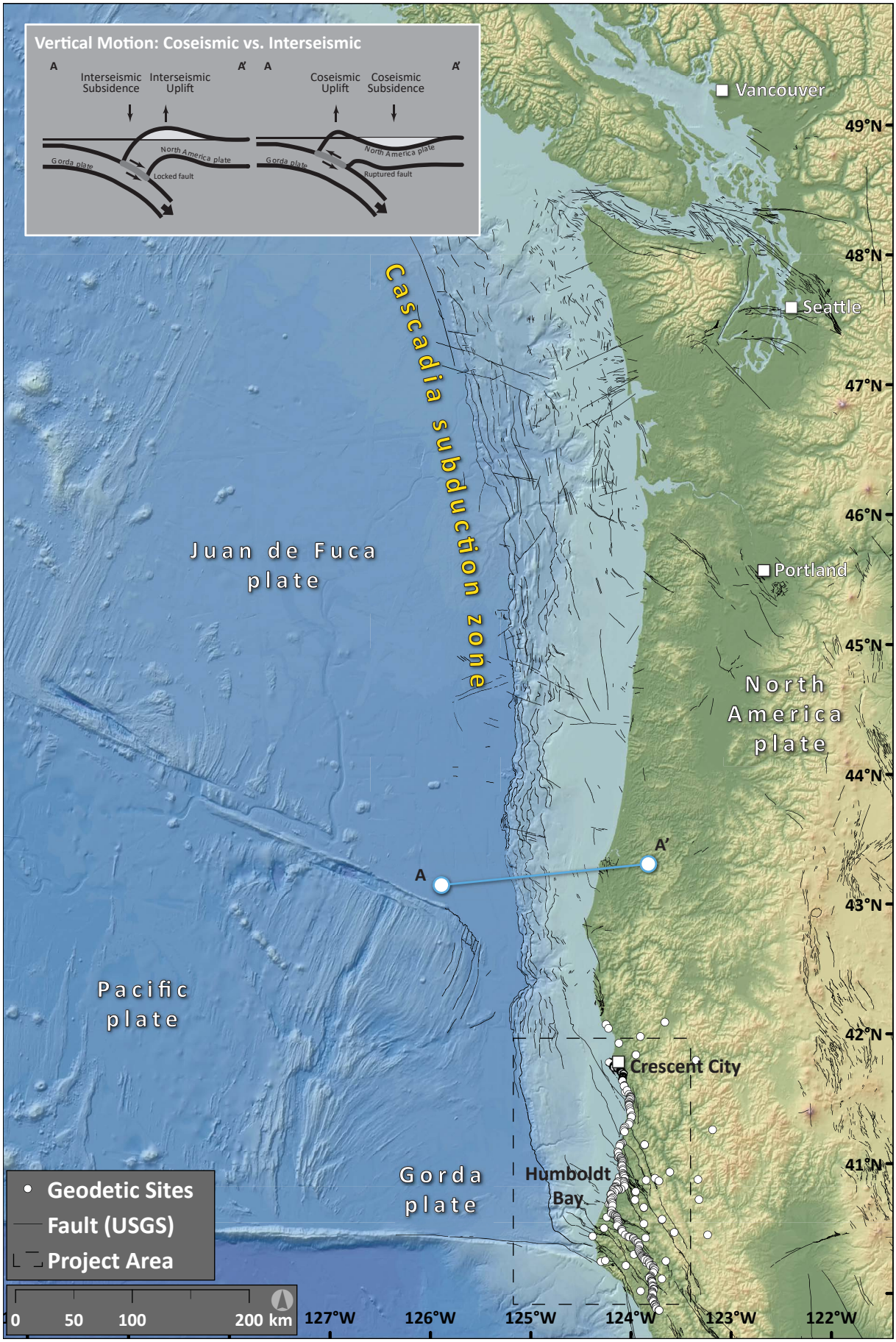

Figure 1 – Cascadia subduction zone map. Tectonic map of plates and the bathymetric expression of the plate boundary faults (elevation data from *Ryan et al.*, 2009). The study region is in the southern part of the subduction zone. Generalized cross section A-A' in across the subduction zone for the interseismic (in-between earthquakes) and coseismic periods (modified from *Plafker*, 1972). USGS faults are plotted in black. Geodetic sites used in this study are plotted as white circles.

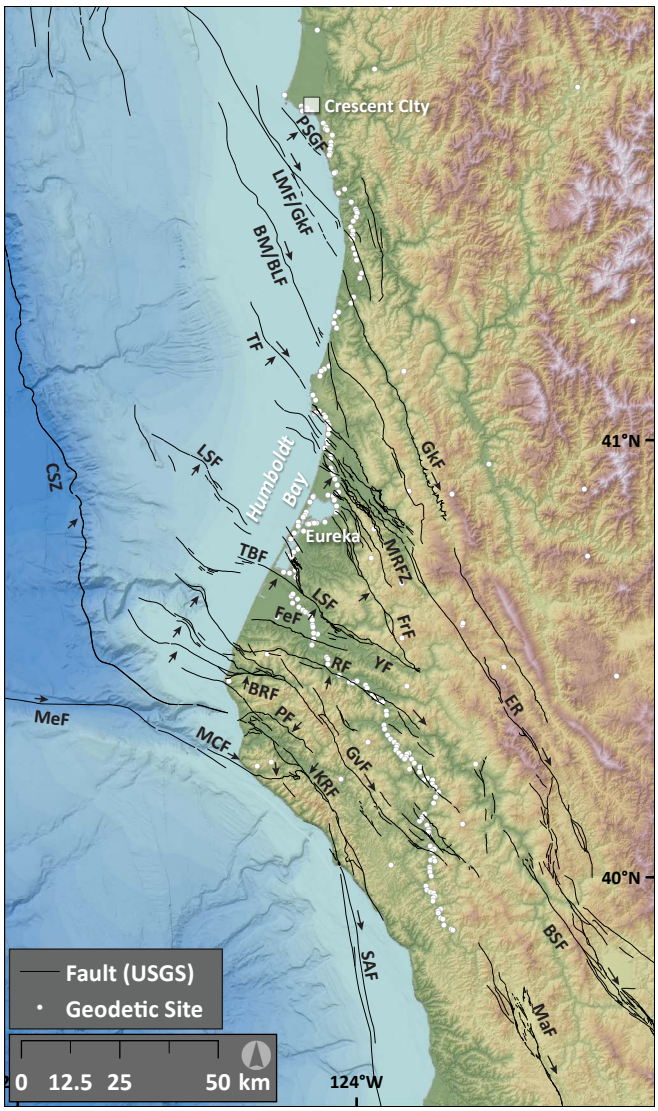

Figure 2 – Mendocino triple junction map. Fault data from USGS Quaternary Active Fault and Fold Database. Fault names: BRF, Bear River; BSF, Bartlett Springs; BM/BLF, Bald Mountain/Big Lagoon; CSZ, Cascadia subduction zone; ER, Eaton Roughs; FeF, Ferndale; FrF, Freshwater; GkF Garlock; GvF, Garberville; KRF, King Range; LM/GF, Lost Man/-Garlock; LSF, Little Salmon; MCF, Mendocino Canyon; MaF Maacama; MeF Mendocino; MRFZ, Mad River; PF, Petrolia; PSGF, Point St. George, RF, Russ in red; TBF, Table Bluff; TF, Trinidad; YF, Yager. Arrows designate direction of fault motion.

combine all 3 independent geodetic site data to estimate decadal scale rates of VLM around the Humboldt Bay region. We also apply a regional estimate of GIA to these geodetic site data to account for ongoing changes in VLM following the last glacial maximum (*Engelhart et al.*, 2015). We also evaluate all geodetic stations for the potential of instability caused by the materials the stations are installed in or on, which includes a qualitative assessment of the mapped geological units.

2.1 Sea-Level Analysis

We analyze mean monthly water level observations at tide stations for CC, Trinidad (TR), and five locations in Humboldt Bay (North Spit, NS; Mad River Slough, MRS; Samoa SO; Fields Landing, FL; Hookton Slough, HS) to estimate the RSL and VLM rates at these sites (Figure 3). We use available data directly from the NOAA websites for all tide stations through December 2021. For the HS site, we installed a temporary tide gage in 2012. For the MRS site, we installed a temporary gage in 2008 and 2016. For the SO and FL gages, we use survey and water level observation data from observations made in 2010 and 2011 by Towill Engineering on the behalf of USACE.

To determine RSL and VLM rate estimates for all stations we follow the general approach of *Burgette et al.* (2009). For the longer record stations (CC, NS and TR) we first remove the mean monthly seasonal cycle from the observations. For stations with adequate data overlap we difference the observations between stations. Differencing the observations removes the regional oceanographic noise common to both stations and the trend of the differences represents the relative crustal uplift rate between stations *Burgette et al.* (2009). Relative rate estimates at each station and the station differences were determined from the slope of a least squares linear regression. We determined uncertainty in the slope estimates as the standard error from the regression adjusted for first-order autocorrelation using the Hildreth-Lu procedure.

To refine the relative rate estimates we combine the individual station rates with the rate differences between stations in a weighted least squares adjustment (*Ghilani*, 2010). The weights (w) were determined as $w = {\sigma_t}^{-2}$, where σ_t is the standard error of the rates, and we selected the standard error of the regression or the standard error from the Hildreth-Lu procedure based on the Durbin -Watson test ($p < 0.05$).

To determine VLM rates at each station we subtract the regional (or absolute) sea level (ReSL) rate (1.99 ± 0.16 mm/year) of *Montillet et al.* (2018) from each station's RSL rate determined by the least squares adjustment. The ReSL standard error of 0.16 mm/year was estimated from the absolute sea level rates reported in Table 3 (*Montillet et al.*, 2018, p. 1206).

2.2 Benchmark Level Analysis

We analyze the available first-order leveling data collected by the NGS, which were observed in 1931, 1945, 1968, and 1988. The leveling data correspond to surveys of benchmarks located along highways that traverse different geology types (Quaternary sediment, Tertiary rocks, and Cretaceous-Tertiary Franciscan mélange rocks). We analyze the unadjusted line data, with orthometric, rod, level, temperature, astronomical, refraction, and magnetic corrections applied by the NGS as appropriate (*United States. Federal Geodetic Control Committee*, 1984). The 1931 and 1945 data pre-date the installation of the NS tide gage. Surveyed benchmarks are generally confined to the route of Highway 101 between Cres-

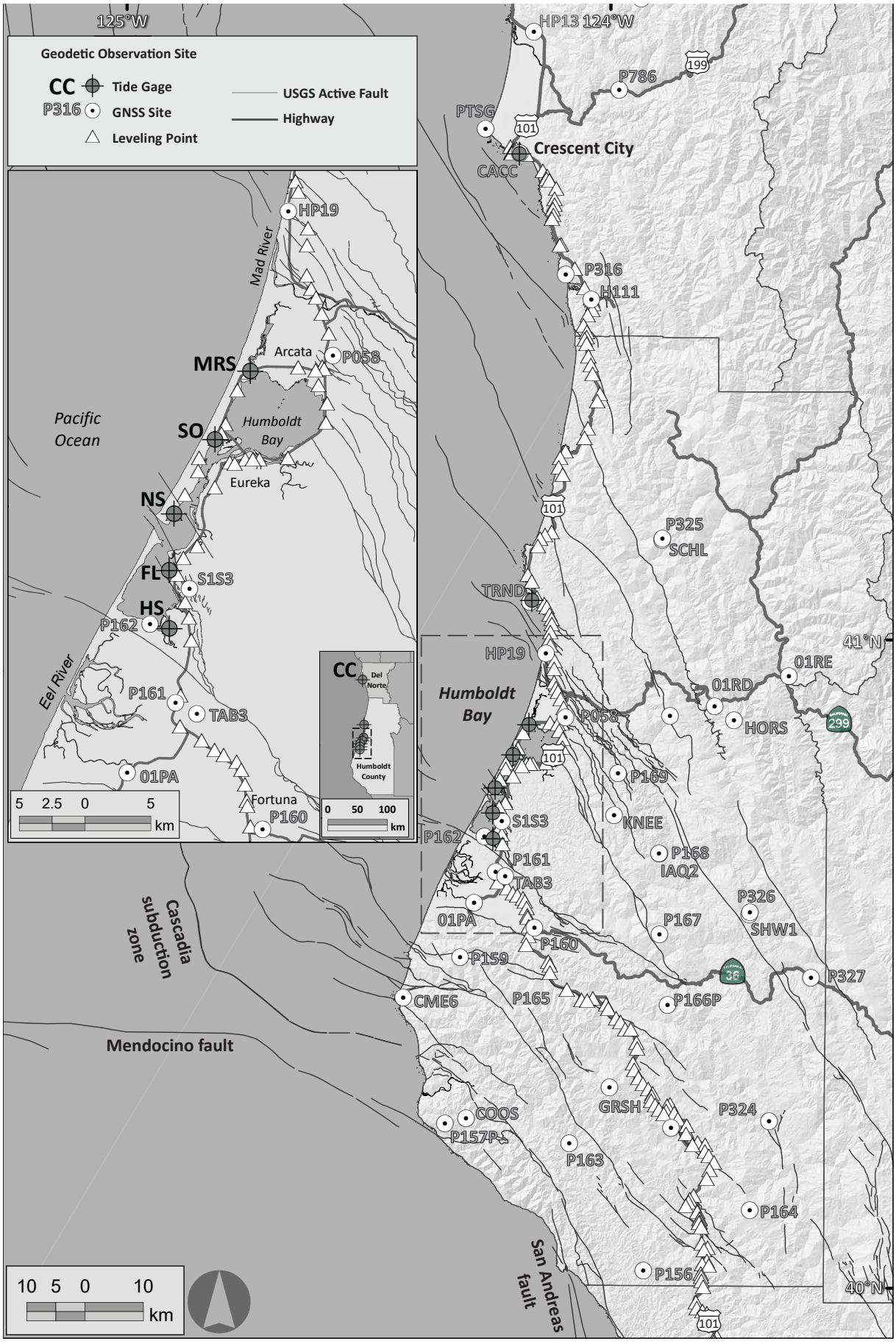

Figure 3 – Geodetic network and fault map for northern California. Geodetic site type is designated by symbol. Shaded relief shows how topography varies across the landscape in the Humboldt Bay region. USGS active fault and fold database is plotted. Inset figure shows tide gage locations in the Humboldt Bay and Crescent City (CC) regions.

cent City south through the Humboldt Bay region. We also analyze data from a spur route between Highway 101 and the NS tide gage that was first observed in 1945 as well as the regional lines observed in 1968 and 1988 (Figure 3). We calculate tilt rates relative to Benchmark 60 in downtown Eureka, which has a long history and appears to be locally stable. Run distance-dependent one sigma errors are propagated following the procedure of *Burgette et al.* (2009).

2.3 GNSS Analysis

Continuously operating GNSS (CGNSS) position data were sourced from the US Geological Survey Northern California and Pacific Northwest continuous GNSS databases. CGNSS stations operated by the National Science Foundation's EarthScope (UNAVCO) and PBO project provide an independent data set to determine rates of VLM (Figure 3). We use the USGS published motion rates for continuously operating GNSS stations in the northern California region surrounding Humboldt Bay. We also include position rate data for campaign GNSS (cGNSS) sites but exclude sites with uncertainties larger than 1 mm/year, which are due to short observation periods. We query rates of motion in north, south, and vertical directions relative to the International Terrestrial Reference System 2014 (ITRF2014) reference frame. Static offsets due to coseismic motion are determined by the USGS and removed from the trend analysis, which modifies the long-term calculated velocities (*Murray and Svarc*, 2017). These static offsets, which also include non-tectonic changes in position, are published by the USGS on the database websites. We use these published velocities for our analyses.

2.4 GIA Model

We incorporate GIA model results from *Engelhart et al.* (2015) to estimate this contribution to the VLM observed at the geodetic sites. We use GIA data from *Engelhart et al.* (2015). The GIA rates for this study range from 1.21 to 1.60 mm/year. We use the square root of the sum of the squares to propagate GIA uncertainty into our results.

2.5 Reference frames

Tide gage data are relative to the station datum (STND) at each tide gage. The STND is unique for each station. We assume that the tidal STND is stable relative to the gage as is reported by NOAA for these stations. Level survey data are also relative to the survey marks surveyed. The GNSS data are relative to the ITRF2014 reference frame. These three data sets are each independent measures of VLM so are not in a shared reference frame.

Table 1 – Observed and adjusted tide station relative sea level rates and differenced relative rate between stations.

Tide Station*	N[†]	RSL[§] or Δ[#] (mm a^{-1})	SE[¥] (mm a^{-1})	AC[‡] (ρ)	SE_{AC}[**] or SE for WLSA[††] (mm a^{-1})	RSL_{ADJ}[§§] or Δ_{ADJ}[##] (mm a^{-1})	SE_{ADJ}[¥¥] (mm a^{-1})
CC	1001	-0.82	0.09	0.46	0.14	-0.84	0.14
TR	129	5.59	1.51	0.60	3.12	2.86	1.10
MRS	10	2.96	1.08	-0.26	1.08	2.53	0.41
SO	12	5.10	1.51	0.46	1.71	3.92	0.35
NS	523	4.89	0.23	0.53	0.42	5.20	0.17
FL	5	3.88	2.44	0.05	2.44	4.65	0.33
HS	21	7.13	1.15	0.39	1.49	6.64	0.65
CC-TR	129	-4.01	0.75	0.53	1.39	-3.69	1.09
CC-MRS	10	-2.99	0.71	0.33	0.75	-3.37	0.40
CC-SO	12	-5.75	1.13	0.76	1.18	-4.76	0.32
CC-NS	522	-6.05	0.06	0.55	0.12	-6.04	0.11
CC-FL	5	-5.19	0.84	-0.75	0.84	-5.49	0.31
CC-HS	21	-7.15	0.70	0.59	0.96	-7.48	0.64
NS-TR	99	4.38	1.18	0.52	2.14	2.34	1.10
NS-MRS	10	2.60	0.51	0.00	0.51	2.67	0.40
NS-SO	10	0.25	1.14	0.72	0.53	1.28	0.31
NS-FL	4	1.29	0.42	-0.65	0.42	0.55	0.30
NS-HS	18	-1.60	0.79	0.40	1.04	-1.45	0.64
SO-FL	5	-0.91	0.20	-0.04	0.20	-0.73	0.19

* Tide Station Abbreviations: Crescent City (CC), Trinidad (TR), Mad River Slough (MRS), Samoa (SO), North Spit (NS), Fields Landing (FL), Hookton Slough (HS)
[†] Number of observations
[§] Relative sea level rate from linear regression, millimeters per year
[#] Differenced relative rate between stations from linear regression
[¥] Estimated standard error from linear regression
[‡] Autocorrelation (ρ = AC parameter)
[**] Standard error adjusted for autocorrelation
[††] Weighted least squares adjustment; SE or SEAC used in WLSA based on Durbin Watson test (p <0.05)
[§§] Relative sea level rate from WLSA
[##] Differenced relative rate from WLSA
[¥¥] Standard error from WLSA

Table 2 – Tide station relative sea level and vertical motion rates.

Tide Station*	RSL_{ADJ}[†] (mm a^{-1})	SE_{ADJ}[§] for RSL_{ADJ} (mm a^{-1})	VLM[#] (mm a^{-1})	SE[#] for VLM (mm a^{-1})	VLM_{GIA}[‡] (mm a^{-1})	SE_{GIA}[¥] (mm^{-1})
CC	-0.84	0.14	2.83	0.21	1.55	0.35
TR	2.86	1.10	-0.87	1.11	-2.29	1.13
MRS	2.53	0.41	-0.54	0.44	-2.01	0.47
SO	3.92	0.35	-1.93	0.38	-3.42	0.41
NS	5.20	0.17	-3.21	0.23	-4.71	0.28
FL	4.65	0.33	-2.66	0.37	-4.18	0.40
HS	6.64	0.65	-4.65	0.67	-6.18	0.69

* Tide Station Abbreviations: Crescent City (CC), Trinidad (TR), Mad River Slough (MRS), Samoa (SO), North Spit (NS), Fields Landing (FL), Hookton Slough (HS)
[†] Relative sea level rate from Weighted least squares adjustment (WLSA)
[§] Standard error from Weighted least squares adjustment (WLSA)
[#] Vertical land motion and standard error; VLM = RSL_{ADJ} - ReSL; ReSL rate of 1.99 mm/yr ± 0.16 mm/yr (*Montillet et al.*, 2018); ReSL = Regional sea level
[‡] VLM rate adjusted for GIA (*Engelhart et al.*, 2015)
[¥] Standard error (SE_{GIA}) for VLM_{GIA}

3 Results

3.1 Water Level Analyses

Table 1 summarizes the rate trend statistics for CC, TR, MRS, SO, NS, FL, and HS. The table also includes the relative rates by differencing all tide gage rates with the CC rates (e.g., CC-TR). Data in the column entitled RSL are from a linear regression and data in the column entitled RSL_{ADJ} are from a weighted least squares analysis (WLSA) of these data.

The RSL rates and associated standard errors (SE) in mm/year from the linear regression, the SE adjusted for autocorrelation, and the adjusted RSL (RSL_{ADJ}) rates and SE from the weighted least squares adjustment (WLSA) for the seven tide gage stations (CC, TR, MRS, SO, NS, FL, and HS) are summarized in Table 1 and Figure 4. Estimated tide gage station VLM rates and SE (Table 2) were determined by differencing the RSL_{ADJ} rate from the absolute sea level rate of 1.99 mm/year (*Montillet et al.*, 2018). GIA adjusted VLM (VLM_{GIA}) rates and SE (Table 2) were estimated by differencing the tide gage VLM and GIA rates of *Engel-*

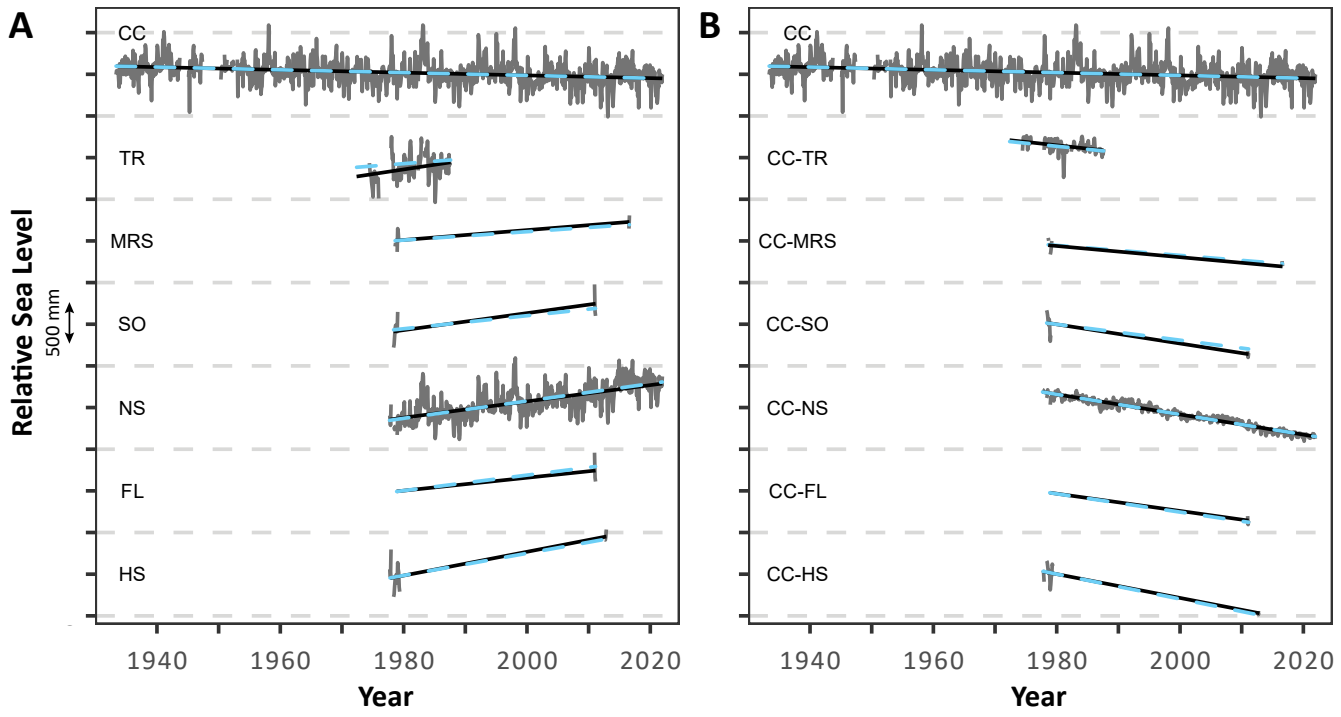

Figure 4 – Tide gage results showing sea-level rise rates. **(A)** National Oceanographic Atmospheric Administration data for each tide gage are presented. Solid lines are linear regression fits. Dashed blue lines are weighted least squares regression rates. CC – Crescent City; TR – Trinidad; MRS – Mad River Slough; SO – Samoa; NS – North Spit; FL – Fields Landing; HS – Hookton Slough. Sites are organized north (top) to south (bottom). **(B)** CC data are plotted for reference as plotted in A. The other tide station data are plotted as the difference between each site and CC, showing how these locations move vertically relative to CC. Note the increase in subsidence from north to south.

hart et al. (2015).

Rates of RSL_{ADJ} for the tide gage stations (in mm/year) are CC (-0.84), TR (2.86), MRS (2.53), SO (3.92), NS (5.20), FL (4.65), and HS (6.64). Estimated rates (in mm/year) of VLM at the station sites are CC (2.83), TR (-0.87), MRS (-0.54), SO (-1.93), NS (-3.21), FL (-2.66), and HS (-4.65). The VLM_{GIA} estimated rates (in mm/year) at the sites are CC (1.55), TR (-2.29), MRS (-2.01), SO (-3.42), NS (-4.71), FL (-4.18), and HS (-6.18).

Table 3 – Comparison between VLM rates in Table 2 and VLM rates interpolated by *Montillet et al.* (2018) and *He et al.* (2022).

Tide Station*	VLM† (mm a^{-1})	SE† for VLM (mm a^{-1})	VLM_M§ (mm a^{-1})	SD# for VLM (mm a^{-1})	Note
CC	2.83	0.35	2.46	0.29	Interpolated
TR	-0.87	1.13	-0.85	0.27	PANGA
MRS	-0.54	0.47			
SO	-1.93	0.41			
NS	-3.21	0.28	-1.15	0.22	Interpolated
FL	-2.66	0.40			
HS	-4.65	0.69			

* Tide Station Abbreviations: Crescent City (CC), Trinidad (TR), Mad River Slough (MRS), Samoa (SO), North Spit (NS), Fields Landing (FL), Hookton Slough (HS)
† Tide station vertical land motion (VLM) and standard error (SE), see Table 2; VLM = RSLADJ - ReSL; ReSL rate of 1.99 mm/yr ± 0.16 mm/yr (*Montillet et al.*, 2018); ReSL = Regional sea level
§ Vertical land motion rate (VLM) linearly interpolated between geodetic sites (*Montillet et al.*, 2018) or published by PANGA (see note)
# Standard deviation (SD) from *Montillet et al.* (2018) or PANGA in *He et al.* (2022) (see note)

We compared our estimated tide gage VLM with those presented in *Montillet et al.* (2018) and *He et al.* (2022) in Table 3. *Montillet et al.* (2018) linearly interpolated VLM rates between geodetic stations for CC and NS, and *He et al.* (2022) present a VLM rate for TR.

3.2 Benchmark Level Analysis

Repeated first-order leveling along coastal highway routes provides spatially dense estimates of uplift/-subsidence rate variation. In the Humboldt Bay area, leveling was completed between the NS tide gage and the main leveling route along Highway 101 in 1945, 1967, and 1988. Relative uplift rates calculated from these epochs are all consistent within estimated random error, showing subsidence of North Spit at approximately 3 mm/year relative to Arcata, and 1.5–2 mm/year relative to benchmarks in downtown Eureka (Benchmark 60; *Burgette et al.*, 2012). VLM rates for the 1988-1967 period are listed in Table SI-1 (Supporting Information).

The main coastal route was surveyed in 1930–1932, then repeated in 1967 and 1988. The uplift rate of the primary (nearest) benchmark at CC relative to the NS primary (nearest) benchmark is 5.61 ± 1.04 mm/year based on differenced 1988 and 1967 surveys (Table 4). This rate estimate overlaps with the 6.04 ± 0.31 mm/year relative uplift of the CC tide gage relative to NS determined from differenced water levels observed above. In contrast, rates of motion between CC and benchmarks in Eureka calculated with the 1930 leveling data and either more recent line show a mismatch of 2.8 to 4.0 mm/year despite lower

Table 4 – Land-level misfit between tide gage and nearest surveymark and GPS sites, including GIA adjustment.

Tide Station*	VLM_{TG}† (mm a^{-1})	SE_{TG}† (mm a^{-1})	Surveymark§	VLM_{SM}# (mm a^{-1})	SE_{SM}# (mm a^{-1})	Dist‡ (km)	GNSS Station¥	VLM_{GNSS}** (mm a^{-1})	SE_{GNSS}** (mm a^{-1})	Dist† (km)	VLM_{SM}§§ misfit (mm a^{-1})	SE_{SM}## misfit (mm a^{-1})	VLM_{GNSS}‡‡ misfit (mm a^{-1})	SE_{GNSS}¥¥ misfit (mm a^{-1} 1)
CC	1.55	0.35	LV0110	1.24	0.93	0.09	CACC	1.32	0.62	0.16	0.31	0.99	0.23	0.71
TR	-2.29	1.13	LV0154	-0.42	0.59	0.99	TRND	-1.65	0.42	0.47	-1.87	1.27	-0.64	1.21
MRS	-2.01	0.47	LV0344	-3.05	0.43	0.00	NA	NA	NA	NA	1.04	0.64	NA	NA
SO	-3.42	0.41	LV0352	-3.64	0.40	0.22	NA	NA	NA	NA	0.22	0.57	NA	NA
NS	-4.71	0.28	LV0361	-4.37	0.46	0.00	NA	NA	NA	NA	-0.34	0.54	NA	NA
FL	-4.18	0.40	LV0263	-3.46	0.47	0.70	S153	-4.08	2.15	2.09	-0.72	0.62	-0.10	2.19
HS	-6.18	0.69	LV0259	-5.56	0.49	1.70	P162	-2.47	0.52	1.52	-0.62	0.85	-3.71	0.86

* Tide Station Abbreviations: Crescent City (CC), Trinidad (TR), Mad River Slough (MRS), Samoa (SO), North Spit (NS), Fields Landing (FL), Hookton Slough (HS)
† Tide station vertical land motion (VLM) and standard error (SE), see Table 2; VLM = RSLADJ - ReSL; ReSL rate of 1.99 mm/yr ± 0.16 mm/yr (*Montillet et al.*, 2018); ReSL = Regional sea level
§ Surveymark identification number
# Surveymark vertical land motion rate (VLM) and standard error (SE)
‡ horizontal distance between tide station and surveymark, kilometers
GNSS station nearest tide station, not applicable (NA) if there is no GNSS station within 2 kilometers
** GNSS vertical land motion rate (VLM) and standard error (SE), millimeters per year
†† horizontal distance between tide station and GNSS station, kilometers
§§ VLM difference between tide station and nearest surveymark, millimeters per year
SE for VLM difference between tide station and nearest surveymark, millimeters per year
‡‡ VLM difference between tide station and nearest GNSS station, millimeters per year
¥¥ SE for VLM difference between tide station and nearest GNSS station, millimeters per year

levels of predicted uncertainty. This comparison relies on the relative uplift rate between the NS primary benchmark and Benchmark 60 in Eureka, estimated from the 1988–67 epoch difference, to estimate the portion of NS to CC route not observed in 1933. However, the rates between Eureka and North Spit are consistent over three epochs from 1945 to 1988, so we interpret that the discrepancy in rates involving the 1930s data results from systematic errors present in the earliest leveling epoch. Based on the agreement with the relative tide gage based VLM, we use rates from differenced 1988 and 1967 leveling as the best estimate of crustal deformation.

3.3 GNSS Analysis

GNSS motion rate analysis results are presented in Table SI-2 (Supporting Information). Site location, observation period, and motion rates are listed for each site relative to the ITRF2014 reference frame. GNSS sites have different observation periods, with the longest record for GNSS site TRND with a time span from 1999-2022. In general, continuous GNSS sites have uncertainties much lower than for campaign GNSS observations. Table SI-3 (Supporting Information) includes information about the static offsets used by the USGS to correct land motion rates for earthquakes, antenna changes, and other factors (*Murray and Svarc*, 2017). These data are published by the USGS for each GNSS station. We present the stability analysis results for all geodetic stations in Supporting Information SI-4.

We compare vertical rates of motion derived from land-level surveys with those derived from GNSS observations and for our tide gage analyses (Table 4). Uplift rates estimated from 1988-1967 leveling epochs are also generally consistent, in a regional sense, with the GNSS results and the relative tidal rates between NS and CC as discussed in the previous section. In general, these independent sites are, within uncertainty, the same rate (Table 4).

Across the region, Humboldt Bay is subsiding while the surrounding areas are not (Figure 5). Rates of VLM are estimated at -4.65 mm/year in south Humboldt Bay, and 2.83 mm/year in Crescent City (Table 2). South of Humboldt Bay there is uplift like the uplift rates north of Humboldt Bay. In Figure 5 we plot outliers without color because these sites (e.g., cGNSS) have large uncertainty an order of magnitude greater than the other sites (e.g., CGNSS), or are not near highway 101, and so make it confusing to visualize the regional pattern of VLM. We include all geodetic sites in Figure SI-5 (Supporting Information).

3.4 Spatial Trends

We present a summary of VLM rates plotted relative to latitude and distance to the CSZ trench, in kilometers (Figure 6). A high-resolution version of Figure 6 is included in Figure SI-6 (Supporting Information). We use a line that represents the subduction zone trench to calculate the distance between each geodetic station to this trench line using the ESRI ArcMap tool "NEAR". These GIS data are listed in the Data Availability section. The longitudinal trends in VLM are plotted in Figure 6A. In the Humboldt Bay region, observation sites to the west are subsiding and observation sites to the east are rising. The same is true for the sites in the lower Eel River Valley, which is slightly closer to the trench but also closer to the southern edge of the CSZ megathrust fault locked zone (*Pollitz and Evans*, 2017). In the Crescent City area observation sites are rising. In southern Humboldt and northern Mendocino counties, observation sites are rising. Some GNSS geodetic sites that appear to be outliers are labeled. Sites with a large uncertainty (such as cGNSS sites) are plotted without error bars. Figure SI-6 (Supporting Information) includes the same plot as Figure 6, but all data are displayed with error bars.

The Latitudinal trends in VLM are plotted in Figure 6B. There is a pronounced region of subsidence in the Humboldt Bay and Eel River Valley regions. Subsidence rates decrease slowly to the north and more rapidly to the south. The latitudinal variation in VLM rates is heterogeneous and appears to have discrete

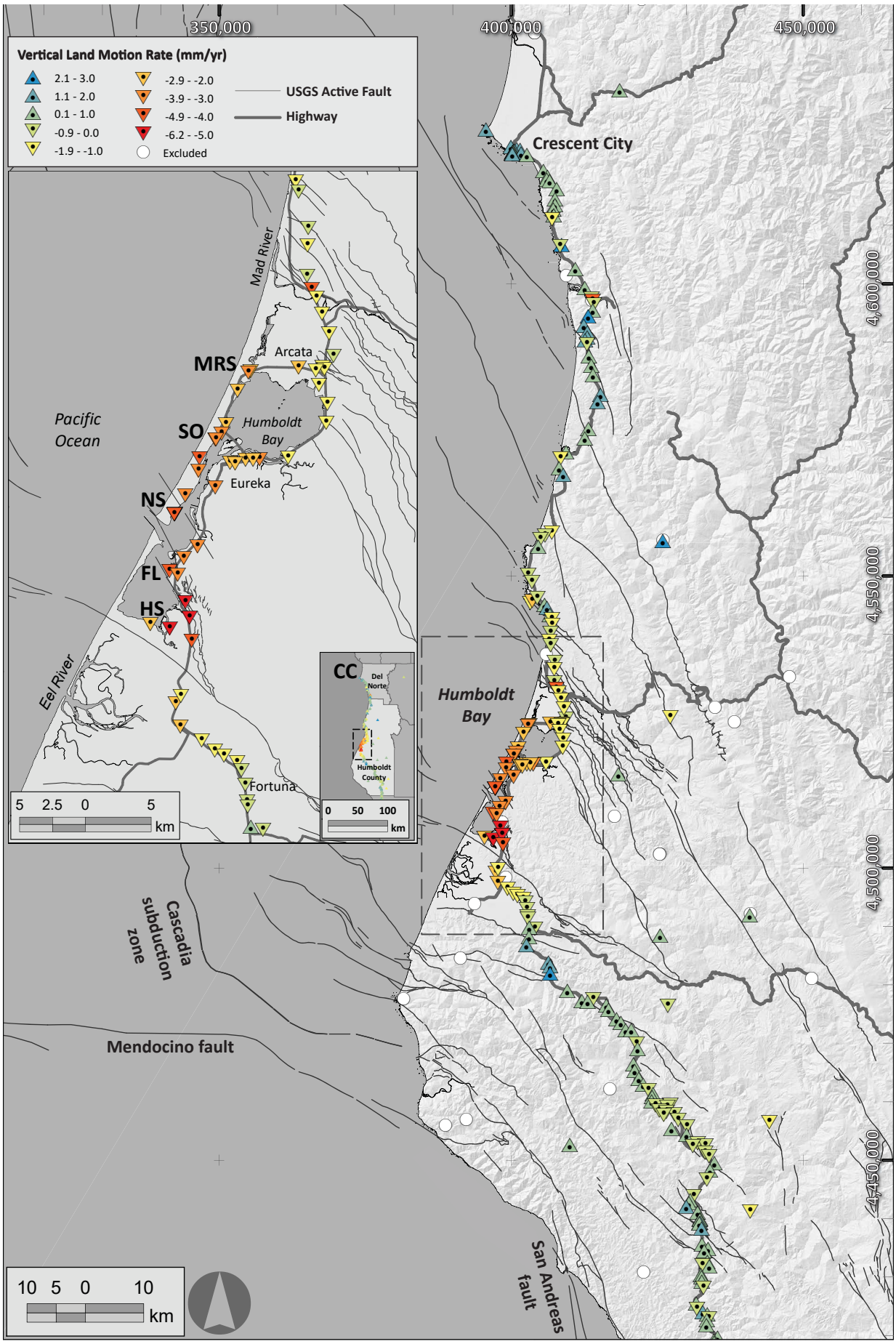

Figure 5 – Geodetic Results. Vertical land-level change in coastal northernmost California. Vertical land motion rates are symbolized with color relative to rate magnitude. Inverted red triangles represent negative uplift and non-inverted blue triangles represent positive uplift. Northing and Easting coordinates are in the UTM NAD83 Zone 10N, meters, reference frame.

Figure 6 – Spatial Variation in Vertical Land Motion. Summary of vertical land-level change in the coastal northernmost California plotted for GNSS, tide gage, and benchmark level sites. Standard error uncertainty is plotted for data used in these analyses. Sites with large uncertainty and sites that are not very close to Highway 101 are plotted without error bars. **(A)** VLM rates (mm/year) plotted relative to horizontal distance (in kilometers) to the CSZ trench, west to east. Only coastal GNSS data are included. Some geodetic sites are labeled. **(B)** VLM rates (mm/year) plotted relative to distance in kilometers (UTM NAD83 Zone 10 N), south to north. A high-resolution version of this figure is presented in Figure SI-6 (Supporting Information).

offsets in several locations. These locations are collocated with crustal faults in the region. Sites near Mad River and Klamath River bridges are subsiding at larger rates than the surrounding sites.

4 Discussion

The subsidence originally interpreted to be locally observed at NS is now found to extend over at least a 100 km^2 area in the Humboldt Bay and Eel River delta regions (Figures 5 and 6). There is a measured spatial variation in vertical land level motion rates across coastal northern California that is contributing to relative sea level observations in the region. This variation is resolved using three independent data sets. Repeated benchmark survey derived uplift rates from 1967-1988 generally agree to within 1 mm/year of tide gage (1977-2012) and GNSS (1999-2019/21/22) derived rates for permanent and temporary sites within Humboldt Bay. Potential sources for the variation include sediment compaction, ground water extraction, glacial isostatic elevation change, and tectonic motion. The results from this study have already been incorporated into sea level rise planning in the county of Humboldt, the cities of Arcata and Eureka, and the communities of Fairhaven, Fields Landing, and King Salmon (*Laird*, 2019).

4.1 Sources for Vertical Land Motion

There are several possible sources for the VLM rates observed in this study, including: subsidence from sediment compaction (*Allen*, 2000); ground water extraction (*Ireland et al.*, 1984), glacial isostatic elevation change (*Shennan et al.*, 2006); geothermal factors (*Massonnet et al.*, 1997); redistribution of lithospheric mantle (*Levandowski and Jones*, 2015), interseismic lithospheric deformation associated with the CSZ, and interseismic deformation associated with crustal faults.

Sediment auto-compaction is a "group of interlinked processes" that cause a sedimentary stratigraphic column to decrease in volume, due to a variety of mechanical and biogeochemical processes (*Allen*, 2000). The amount of compaction can be estimated in several ways, with the magnitude typically presented as a percentage of the original sediment thickness (*Bird et al.*, 2004). Sediment auto-compaction and sea-level rise are both considered responsible for how salt marshes build upward, providing accommodation space (*Allen*, 2000). Different earth materials have different potential for compaction rates (*Stouthamer and van Asselen*, 2015). Various processes and factors that contribute to compaction rates include consolidation (extraction of water from pore space in the sediment) and creep (the viscous movement of sediment and sedimentary particles). *Brain* (2015) reviews these factors and how they contribute to sediment compaction observed in coastal settings. Given that the results presented in this study span sites that are located in both sedimentary settings (tide gage and benchmark sites), as well as bedrock settings (GNSS and benchmark sites), sediment auto-compaction may not be a first order control for the variation in VLM rates presented here (see SI-4 in Supporting Information for more discussion about how geology type may influence our observations).

Land subsidence as a result of ground water extraction has been observed in the central valley of California for decades (*Ireland et al.*, 1984) and is primarily caused by the collapse of pores as the water is removed and pumped to the surface for agricultural activities (*Galloway et al.*, 1998; *Farr and Liu*, 2014). For the same reasons we present above, ground water extraction is probably not a first order control for the variation in VLM rates in our data sets. Though we cannot rule this out as a secondary factor.

Glacial cycles are a major component of the hydrologic cycle at the time scales of centuries to millennia as these cycles lead to the largest redistribution of mass across the globe, in addition to a major contributor to sea level change (*Shackleton*, 1987; *Milne*, 2015). This redistribution of mass leads to increased mass in regions of ice cover (generally in continental settings) during glacial periods and concomitant reduction of mass in oceanic regions (where the majority of water for the ice comes from). This redistribution, known as glacial isostatic adjustment (GIA), leads to subsidence in ice-covered regions during glacial periods, and uplift in these same regions during interglacial periods (*Peltier*, 1990, 1999). The contribution of GIA to projections of sea-level rise has been evaluated for the east coast of North America (*Love et al.*, 2016) and records of past sea-level rise on the west coast (*Shugar et al.*, 2014) of North America.

There have been several estimates of the contribution of GIA to sea-level rise in the Humboldt Bay region (*Long and Shennan*, 1998; *Engelhart et al.*, 2015). Due to the latitudinal proximity to the Cordilleran Ice Sheet during the Last Glacial Maximum, there exists a latitudinal variation to GIA rates of VLM. *Long and Shennan* (1998) estimated this gradient to be 0.25 $\pm$ 0.02 mm/year per 100 km. *Engelhart et al.* (2015) use sea level index points from mid- to late-Holocene stratigraphy to estimate the spatial variation in GIA for the northern pacific coast of North America. GIA VLM rates range from $+0.7 \pm 0.8$ mm/year in Canada to -1.5 ± 0.3 mm/year in northern California. Their revised VLM rate gradient is between 0.1 and 0.15 mm/year per 100 km. In the Humboldt Bay region, the GIA contribution to SLR may be about 1.5, 1.4, and 1.3 mm/year at Eel River, Arcata Bay, and Crescent City respectively (*Engelhart et al.*, 2015). While the rates of GIA derived SLR are significant, and contribute to the overall SLR rates, there is not a large variation in GIA across this region (about 0.2 mm/year). GIA effects are superposed on tectonic deformation, and enhances relative sea level rise in southern Cascadia, and further diminishes relative sea level rise in northern Cascadia. The VLM rates

plotted in Figures 5 and 6, Supporting Information SI-4, and Figures SI-5 and SI-6, and data presented in Tables 2 and 4, include these GIA adjustments.

4.2 Tectonic Deformation Sources in Northern California

There exists evidence elsewhere along the CSZ margin for interseismic tectonic deformation (*Mitchell et al.*, 1994; *Hyndman and Wang*, 1995), principally due to subduction zone tectonics. Some models of the subduction zone assumed regions of homogeneous seismogenic locking on the megathrust fault (*Flück et al.*, 1997; *Wang et al.*, 2003). However, there is support for spatial variation in the seismogenic coupling along the fault as evidenced by geodetic data (*Mitchell et al.*, 1994; *Verdonck*, 2006; *McCaffrey et al.*, 2013), which may explain the variation in VLM rates found in benchmark survey studies in Oregon (*Burgette et al.*, 2009) and Washington (*Newton et al.*, 2021), as well as in studies that also incorporate continuous GNSS time series and episodic tremor location analysis (*Schmalzle et al.*, 2014). Additional sources for spatial variation in VLM rates could be tectonic deformation associated with crustal faults in the North America or Gorda plates. Coseismic horizontal motion has been observed at GNSS sites because of Gorda intraplate earthquakes (evidence for seismogenic locking of the megathrust; *Williams and McPherson*, 2006). Because these faults are strike-slip, and there has been no observed coseismic vertical motion across these faults, there is probably a low likelihood these faults would produce measurable VLM at the decadal scale. However, most of the North America plate crustal faults are thrust or reverse faults.

The Quaternary fold and thrust belt associated with the accretionary prism of the CSZ comes on land in the region of Humboldt Bay (*Clarke and Carver*, 1992). Additional crustal faults in the region are associated with the northern migration of the Sierra Nevada Block *Williams et al.* (2006). Faults in the Mad River fault zone, Little Salmon fault zone, and the Russ and Bear River fault zones strike across the geodetic sites used in this study. These faults are compressional thrust or reverse faults, which may cause interseismic VLM. However, there may be some component of oblique slip on these faults in the Humboldt Bay region due to the northern migration of the Sierra Nevada block and the Mendocino triple junction (*Williams et al.*, 2006).

Not all of these faults have been evaluated for Holocene activity nor do they all have slip rates. Given the known slip rates, the Little Salmon fault has the highest paleoseismic slip rate in the region, approximately 6 mm/year (*Carver and Burke*, 1988; *McCrory*, 1996, 2000). The Mad River and Little Salmon fault zones deform Pleistocene landforms likely associated with strain associated with the CSZ but may also respond to the San Andreas fault system (*Williams et al.*, 2006). Further south, the Russ fault and Bear River fault zone are oriented with a more easterly strike so may accommodate the northward propagating Sierra Nevada block (north-south compression), but also may have oblique slip along the southeasterly portions of these faults.

The spatial variation in VLM rates shown in Figure 6 helps us visualize first and possibly second order controls for deformation in this region. We include all tide gage and level data points but limit the plot to the GNSS sites closest (relative to trench distance) to the other two data sets.

VLM rates in Figure 6A show a westward-down trend in VLM rates in the Humboldt Bay region. This westward-down, eastward-up trend is most easily explained by the seismogenic coupling of the CSZ megathrust and the elastic flexure of the North America plate lithosphere as modelled by *Hyndman and Wang* (1995), *Wang et al.* (2003), and *Newton et al.* (2021). The locked fault is pulling the lithosphere downwards in the west and, eastward of the locked zone, presumably the NAP is compressed and possibly warping upwards in the east. Sites in Crescent City are more landward, relative to the locked fault, than the sites in the Humboldt Bay region. This is indicative of the distance to the trench, which is further offshore of Crescent City. This explains why the Crescent City sites have a positive VLM rate relative to Humboldt Bay, presuming the dip of the megathrust is similar and the along-dip seismogenic coupling pattern is similar between these locations (e.g., *Schmalzle et al.*, 2014; *Pollitz and Evans*, 2017). The sites to the southeast of the Humboldt Bay region have relative positive VLM rates and these are unrelated to CSZ tectonics since they span the southern edge of the Gorda plate, so may not directly influenced by the CSZ. There are some outlier sites, but their regional misfit may be explained in some cases based upon their location. GNSS sites CME6 and P159 (Figure 3) are located far to the west of the level-line (i.e., highway 101) and tide gage data. Because these sites are closer to the megathrust fault tip (i.e., closer to the trench), they have negative VLM rates (Figure 6B). P169 is a GNSS site far to the east of the level data, so has a larger positive VLM rate than the level data because it is further away from the megathrust fault tip (Figure 6B). Other example GNSS sites that are not proximal to highway 101 are also labeled and one can see their location plotted on Figure 3 and their rates on Figure 6.

There are some data point locations that are outliers with no obvious explanation. GNSS site P316 and level mark sites located near Mad River and Klamath River, show VLM rates that are different from their surrounding data. The GNSS site P316 VLM rate is based upon a different time period than the level data, which may explain the different rate. Though there remains uncertainty about the cause of this difference in VLM rate. The level sites near these two rivers may not be in stable locations, which may explain the different rate. Perhaps the abutments of the river bridges may be causing subsidence at these lo-

cations. Other outlier sites are labeled and are excluded due to the large rate uncertainty, usually because they are cGNSS sites (see the large error bars in Figure SI-6, Supporting Information). Some sites are excluded because they are far away from Highway 101, so make the visualization of the regional down warping difficult to interpret. We do include the entire set of data in map and profile views in Figures SI-5 and SI-6 (Supporting Information).

Preliminary analysis from *Blackwell et al.* (2020), using interferometric synthetic aperture radar (INSAR) data, shows that there is considerable variation in geodetic motion across the landscape. However, these data show rates of subsidence that span the uplands north of the lower Eel River Valley and the floodplain of the lower Eel River Valley without a change in VLM rate (suggesting that these VLM rates are not due to factors related to geology like sediment compaction or changes in groundwater levels).

Using tide gage, benchmark level, and GNSS observations to characterize the interseismic plate tectonic land-level change associated with the southern Cascadia subduction zone (CSZ), we provide fundamental sea-level rise data for making management decisions as they apply to coastal landscapes. These data are already being incorporated into hydrodynamic modeling and inundation vulnerability mapping for the Humboldt Bay area (Anderson, 2015) and used as a basis for the Humboldt Bay Area Plan for Sea Level Rise Vulnerability Assessment (*Laird*, 2018). The next step in this process is to develop a viscoelastic model of this tectonic deformation so that we may interpolate sea level change for un-observed locations. Within this framework we will also be able to assess future coseismic VLM impacts.

5 Conclusion

Trends of sea-level rise at the NS tide gage, previously thought to be anomalous compared to the CC tide gage, are consistent with other observations in Humboldt Bay and resolvable when included in our regional analyses. The observed gradients in tectonic deformation directly control the variation of sea-level rise in this region. However, the detailed spatial variation of vertical land-level motion rates remains unresolved in some parts of the Humboldt Bay region (between the geodetic observation sites).

We conclude that tide gage, GNSS, and land-level survey data provide independent observations of tectonic deformation in Northern California which is the reason for some of the highest and lowest rates of sea level rise along the coasts of California, Oregon, and Washington. We conclude that the principal source for the variation in VLM rates across coastal northern California is due to interseismic deformation associated with both the CSZ and with North America crustal faults. We cannot preclude a secondary effect from interseismic deformation across the lower slip rate crustal faults in the region nor from additional variation from non-tectonic sources. We note that these geodetic data span over a half a century (1967-2022), and these rates are consistent across the different geodetic methods that span different time periods. This suggests that the megathrust earthquake cycle has not changed significantly enough to cause changes in VLM rate. However, we won't really know about the influence that the CSZ earthquake cycle has on these geodetic data until there is an interface event. Additional work needs to be conducted to learn more about the potential for non-tectonic sources of deformation. However, preliminary analysis from *Blackwell et al.* (2020) suggest that, for some places, these VLM rates are not due to factors related to geology.

Acknowledgements

Parts of this research was funded by the U.S. Fish and Wildlife Service with funds that came from the North Pacific and California Landscape Conservation Cooperatives. We would also like to thank the contributions of local, county, state, and federal agencies, organizations, private consultants, and students from the Cal Poly Humboldt, Department of Geology. We appreciate the two volunteer reviewers of this article.

Author Contributions

Jason R. Patton wrote paper, prepared figures and tables, worked on GNSS data, compiled data, participated in field work. Todd B. Williams formed our collaborative group, worked on GNSS data, participated in field work , reviewed paper. Jeffrey K. Anderson conducted campaign tide gage deployments, performed tide gage analysis, participated in field work, reviewed paper. Mark Hemphill-Haley participated in field work, reviewed paper. Robert C. McPherson participated in field work, reviewed paper. Tom H. Leroy participated in field work, reviewed paper. Reed J. Burgette participated in field work, conducted benchmark level analyses, reviewed paper. Ray J. Weldon participated in field work, reviewed paper.

Supporting Information

Supporting Information Table SI-1 includes VLM rate data for each benchmark monument site used in this paper. Supporting Information Table SI-2 includes VLM rate data for each GNSS site used in this paper. Supporting Information Table SI-3 static offsets applied by the USGS to each GNSS site used in this paper. Supporting Information File SI-4, Evaluation of site and monument stability provides a summary of our evaluation of each site relative to the geological unit type and site stability index. Supporting Information Figure SI-5 includes a map, like in Figure 5 but includes all geodetic sites. Supporting Information Figure SI-6 includes plots of geodetic data vs. trench distance and latitude, like in Figure 6. The first page in-

cludes a high-resolution version of Figure 6 and the second page is the same figure as the first page but includes uncertainty bars for all geodetic data.

Data Availability

Data from this research are posted on Zenodo https://doi.org/10.5281/zenodo.7420441. These data include a GIS ESRI shapefile for the geodetic stations and a GIS ESRI shapefile that shows the location of the subduction zone trench that we used to calculate trench distance for each geodetic station. These data also include the tables in a spreadsheet format. We also include all Supporting Information files.

Fault GIS data are acquired as GIS downloads from the U.S. Geological Survey Quaternary Fault and Fold database as downloaded 11 December 2017 from https://www.usgs.gov/programs/earthquake-hazards/faults.

U.S. Geological Survey, Quaternary fault and fold database for the United States, accessed December 11, 2017, at: https://www.usgs.gov/natural-hazards/earthquake-hazards/faults, https://doi.org/10.3133/fs20043033.

GNSS data are downloaded from websites listed in the GIS database posted on Zenodo. The three main USGS websites are the Northern California network (e.g., https://earthquake.usgs.gov/monitoring/gps/NCalifornia/p165#itrf2008), the Pacific Northwest Network (https://earthquake.usgs.gov/monitoring/gps/Pacific_Northwest_ITRF2014), and the ITRF2014 Northern California network (https://earthquake.usgs.gov/monitoring/gps/NCalifornia_SGPS_ITRF2014).

Tide gage data are downloaded from the NOAA website Tides and Currents: https://tidesandcurrents.noaa.gov/stations.html?type=Water+Levels.

Surveymark data were obtained by visiting the Silver Spring, Maryland (USA) National Geodetic Survey (NGS) office where survey notes are archived. In addition, surveymark datasheets can be downloaded from the NGS website https://geodesy.noaa.gov/datasheets/.

Competing Interests

The authors declare no competing interests.

Peer Review

This publication was peer-reviewed by Raphael Grandin and Romain Jolivet. The full peer-review report can be found here: https://tektonika.online/index.php/home/article/view/6/3.

Copyright Notice

References

Allen, J. R. L. (2000), Morphodynamics of holocene salt marshes: a review sketch from the atlantic and southern north sea coasts of europe, *Quaternary science reviews*, *19*(12), 1155–1231, doi: 10.1016/S0277-3791(99)00034-7.

Bird, M. I., L. K. Fifield, S. Chua, and B. Goh (2004), Calculating sediment compaction for radiocarbon dating of intertidal sediments, *Radiocarbon*, *46*(1), 421–435, doi: 10.1017/S0033822200039734.

Blackwell, E., M. Shirzaei, C. Ojha, and S. Werth (2020), Tracking california's sinking coast from space: Implications for relative sea-level rise, *Science advances*, *6*(31), eaba4551, doi: 10.1126/sciadv.aba4551.

Brain, M. J. (2015), Compaction, in *Handbook of Sea-Level Research*, pp. 452–469, John Wiley & Sons, Ltd, Chichester, UK, doi: 10.1002/9781118452547.ch30.

Burgette, R. J., R. J. Weldon, II, and D. A. Schmidt (2009), Interseismic uplift rates for western oregon and along-strike variation in locking on the cascadia subduction zone, *Journal of geophysical research*, *114*(B1), doi: 10.1029/2008jb005679.

Burgette, R. J., R. J. Weldon, D. A. Schmidt, and T. B. Williams (2012), Constraints on interseismic locking along the southern cascadia subduction zone from historic and recent leveling and sea level observations, in *American Geophysical Union, Fall Meeting*, vol. 2012, pp. T23E–2719.

Carver, G. A., and R. M. Burke (1988), Trenching investigations of northwestern california faults, humboldt bay region, *Tech. rep.*, USGS.

Cazenave, A., and W. Llovel (2010), Contemporary sea level rise, *Annual review of marine science*, *2*, 145–173, doi: 10.1146/annurev-marine-120308-081105.

Church, J., J. Gregory, N. White, S. Platten, and J. Mitrovica (2011), Understanding and projecting sea level change, *Oceanography*, *24*(2), 130–143, doi: 10.5670/oceanog.2011.33.

Church, J. A., P. U. Clark, A. Cazenave, J. M. Gregory, S. Jevrejeva, A. Levermann, M. A. Merrifield, G. A. Milne, R. S. Nerem, P. D. Nunn, A. J. Payne, W. T. Pfeffer, D. Stammer, and A. S. Unnikrishnan (2013), Sea level change, in *Climate Change 2013: The Physical Science Basis. Contribution of Working Group I to the Fifth Assessment Report of the Intergovernmental Panel on Climate Change*, edited by T. F. Stocker, D. Qin, G.-K. Plattner, M. Tignor, S. K. Allen, J. Boschung, A. Nauels, and Xia, Y, Bex, V, Midgley, P M, pp. 1137–1216, Cambridge University Press, Cambridge, United Kingdom and New York, NY, USA.

Clark, J. A., W. E. Farrell, and W. Richard Peltier (1978), Global changes in postglacial sea level: A numerical calculation, *Quaternary Research*, *9*(3), 265–287, doi: 10.1016/0033-5894(78)90033-9.

Clarke, S. H., Jr, and G. A. Carver (1992), Late holocene tectonics and paleoseismicity, southern cascadia subduction zone, *Science*, *255*(5041), 188–192, doi: 10.1126/science.255.5041.188.

Engelhart, S. E., M. Vacchi, B. P. Horton, A. R. Nelson, and

R. E. Kopp (2015), A sea-level database for the pacific coast of central north america, *Quaternary science reviews*, *113*, 78–92, doi: 10.1016/j.quascirev.2014.12.001.

Farr, T. G., and Z. Liu (2014), Monitoring subsidence associated with groundwater dynamics in the central valley of california using interferometric radar, in *Remote Sensing of the Terrestrial Water Cycle*, pp. 397–406, John Wiley & Sons, Inc, Hoboken, NJ, doi: 10.1002/9781118872086.ch24.

Feng, L., A. V. Newman, M. Protti, V. González, Y. Jiang, and T. H. Dixon (2012), Active deformation near the nicoya peninsula, northwestern costa rica, between 1996 and 2010: Interseismic megathrust coupling, *Journal of Geophysical Research*, *117*(B6), doi: 10.1029/2012JB009230.

Flück, P., R. D. Hyndman, and K. Wang (1997), Three-dimensional dislocation model for great earthquakes of the cascadia subduction zone, *Journal of geophysical research*, doi: 10.1029/97JB01642.

Galloway, D. L., K. W. Hudnut, and others (1998), Detection of aquifer system compaction and land subsidence using interferometric synthetic aperture radar, antelope valley, mojave desert, california, *Water Resources*, doi: 10.1029/98WR01285.

Gehrels, R. (2010), Sea-level changes since the last glacial maximum: An appraisal of the IPCC fourth assessment report, *Journal of Quaternary Science*, *25*(1), 26–38, doi: 10.1002/jqs.1273.

Ghilani, C. D. (2010), *Adjustment Computations: Spatial Data Analysis*, John Wiley & Sons.

He, X., J.-P. Montillet, R. Fernandes, T. I. Melbourne, W. Jiang, and Z. Huang (2022), Sea level rise estimation on the pacific coast from southern california to vancouver island, *Remote Sensing*, *14*(17), 4339, doi: 10.3390/rs14174339.

Horton, B. P., S. Rahmstorf, S. E. Engelhart, and A. C. Kemp (2014), Expert assessment of sea-level rise by AD 2100 and AD 2300, *Quaternary science reviews*, *84*, 1–6, doi: 10.1016/j.quascirev.2013.11.002.

Hyndman, R. D., and K. Wang (1995), The rupture zone of cascadia great earthquakes from current deformation and the thermal regime, *Journal of geophysical research*, *100*(B11), 22,133–22,154, doi: 10.1029/95jb01970.

Ireland, R. L., J. F. Poland, and F. S. Riley (1984), Land subsidence in the san joaquin valley, california, as of 1980, doi: 10.3133/pp437i.

Jevrejeva, S., A. Grinsted, and J. C. Moore (2009), Anthropogenic forcing dominates sea level rise since 1850, *Geophysical research letters*, *36*(20), doi: 10.1029/2009gl040216.

King, M. A., M. Keshin, P. L. Whitehouse, and others (2012), Regional biases in absolute sea-level estimates from tide gauge data due to residual unmodeled vertical land movement, *Geophysical*, doi: 10.1029/2012GL052348.

Komar, P. D., J. C. Allan*, and P. Ruggiero (2011), Sea level variations along the u.s. pacific northwest coast: Tectonic and climate controls, *Journal of Coastal Research*, *276*, 808–823, doi: 10.2112/jcoastres-d-10-00116.1.

Laird, A. (2018), Humboldt bay area plan communities at risk sea level rise vulnerability assessment, *Tech. rep.*, Humboldt State University.

Laird, A. (2019), Humboldt bay area plan communities at risk strategic sea level rise adaptation planning report, *Tech. rep.*, Humboldt State University.

Lambeck, K., and J. Chappell (2001), Sea level change through the last glacial cycle, *Science*, *292*(5517), 679–686, doi: 10.1126/science.1059549.

Levandowski, W., and C. H. Jones (2015), Linking sierra nevada, california, uplift to subsidence of the tulare basin using a seismically derived density model, *Tectonics*, *34*(11), 2349–2358, doi: 10.1002/2015tc003824.

Long, A. J., and I. Shennan (1998), Models of rapid relative sea-level change in washington and oregon, USA, *Holocene*, *8*(2), 129–142, doi: 10.1191/095968398666306493.

Love, R., G. A. Milne, L. Tarasov, S. E. Engelhart, M. P. Hijma, K. Latychev, B. P. Horton, and T. E. Törnqvist (2016), The contribution of glacial isostatic adjustment to projections of sea-level change along the atlantic and gulf coasts of north america, *Earth's future*, *4*(10), 440–464, doi: 10.1002/2016ef000363.

Loveless, J. P., and B. J. Meade (2010), Geodetic imaging of plate motions, slip rates, and partitioning of deformation in japan, *Journal of geophysical research*, *115*(B2), doi: 10.1029/2008jb006248.

Massonnet, D., T. Holzer, and H. Vadon (1997), Land subsidence caused by the east mesa geothermal field, california, observed using SAR interferometry, *Geophysical research letters*, *24*(8), 901–904, doi: 10.1029/97gl00817.

McCaffrey, R., A. I. Qamar, R. W. King, R. Wells, G. Khazaradze, C. A. Williams, C. W. Stevens, J. J. Vollick, and P. C. Zwick (2007), Fault locking, block rotation and crustal deformation in the pacific northwest, *Geophysical Journal International*, *169*(3), 1315–1340, doi: 10.1111/j.1365-246X.2007.03371.x.

McCaffrey, R., R. W. King, S. J. Payne, and others (2013), Active tectonics of northwestern US inferred from GPS-derived surface velocities, *Journal of geophysical research*, doi: 10.1029/2012JB009473.

McCrory, P. A. (1996), Evaluation of fault hazards, northern coastal california, *Tech. Rep. 96-656*, U.S. Geological Survey, doi: 10.3133/ofr96656.

McCrory, P. A. (2000), Upper plate contraction north of the migrating mendocino triple junction, northern california: Implications for partitioning of strain, *Tectonics*, *19*(6), 1144–1160, doi: 10.1029/1999tc001177.

McKenzie, K. A., and K. P. Furlong (2021), Isolating non-subduction-driven tectonic processes in cascadia, *Geoscience Letters*, *8*(1), 1–12, doi: 10.1186/s40562-021-00181-z.

Milne, G. A. (2015), Glacial isostatic adjustment, in *Handbook of Sea-Level Research*, edited by I. Shennan, A. J. Long, and B. P. & Horton, pp. 419–437, John Wiley & Sons, Ltd, Chichester, UK, doi: 10.1002/9781118452547.ch28.

Mitchell, C. E., P. Vincent, R. J. Weldon, II, and M. A. Richards (1994), Present-day vertical deformation of the cascadia margin, pacific northwest, united states, *Journal of geophysical research*, *99*(B6), 12,257–12,277, doi: 10.1029/94jb00279.

Montillet, J.-P., T. I. Melbourne, and W. M. Szeliga (2018), GPS vertical land motion corrections to sea-level rise estimates in the pacific northwest, *Journal of Geophysical Research: Oceans*, *123*(2), 1196–1212, doi: 10.1002/2017jc013257.

Murray, J. R., and J. Svarc (2017), Global positioning system data collection, processing, and analysis conducted by the U.S. geological survey earthquake hazards program, *Seismological Research Letters*, *88*(3), 916–925, doi: 10.1785/0220160204.

Nelson, A. R., I. Shennan, and A. J. Long (1996), Identifying coseismic subsidence in tidal-wetland stratigraphic sequences at the cascadia subduction zone of western north america, *Journal of geophysical research*, *101*(B3), 6115–6135, doi: 10.1029/95jb01051.

Nerem, R. S., D. P. Chambers, C. Choe, and G. T. Mitchum (2010), Estimating mean sea level change from the TOPEX and jason altimeter missions, *Marine Geodesy*, *33*(sup1), 435–446, doi: 10.1080/01490419.2010.491031.

Newton, T. J., R. Weldon, I. M. Miller, D. Schmidt, G. Mauger, H. Morgan, and E. Grossman (2021), An assessment of vertical land movement to support coastal hazards planning in washington state, *WATER*, *13*(3), 281, doi: 10.3390/w13030281.

Nicholls, R. (2011), Planning for the impacts of sea level rise, *Oceanography*, *24*(2), 144–157, doi: 10.5670/oceanog.2011.34.

Nicholls, R. J., and A. Cazenave (2010), Sea-level rise and its impact on coastal zones, *Science*, *328*(5985), 1517–1520, doi: 10.1126/science.1185782.

Patton, J. R., T. B. Williams, J. Anderson, R. Burgette, and T. Leroy (2014), Tectonic land level changes and their contribution to sea-level rise, humboldt bay region, northern california: 2014 status update, *Tech. rep.*, Cascadia GeoSciences.

Patton, J. R., T. Williams, J. Anderson, and T. Leroy (2017), Tectonic land level changes and their contribution to sea-level rise, humboldt bay region, northern california, *Tech. rep.*, Humboldt State University.

Peltier, W. R. (1976), Glacial-Isostatic Adjustment—II. the inverse problem, *Geophysical Journal International*, *46*(3), 669–705, doi: 10.1111/j.1365-246X.1976.tb01253.x.

Peltier, W. R. (1990), *Glacial isostatic adjustment and relative sea-level change*, 73–87 pp., National Academies Press, Washington D.C.

Peltier, W. R. (1999), Global sea level rise and glacial isostatic adjustment, *Global and planetary change*, *20*(2), 93–123, doi: 10.1016/S0921-8181(98)00066-6.

Peltier, W. R. (2002), Global glacial isostatic adjustment: palaeogeodetic and space-geodetic tests of the ICE-4G (VM2) model, *Journal of Quaternary Science*, *17*(5-6), 491–510, doi: 10.1002/jqs.713.

Peltier, W. R., and R. G. Fairbanks (2006), Global glacial ice volume and last glacial maximum duration from an extended barbados sea level record, *Quaternary science reviews*, *25*(23), 3322–3337, doi: 10.1016/j.quascirev.2006.04.010.

Plafker, G. (1972), Alaskan earthquake of 1964 and chilean earthquake of 1960: Implications for arc tectonics, *Journal of geophysical research*, *77*(5), 901–925, doi: 10.1029/jb077i005p00901.

Pollitz, F. F., and E. L. Evans (2017), Implications of the earthquake cycle for inferring fault locking on the cascadia megathrust, *Geophysical Journal International*, *209*(1), 167–185, doi: 10.1093/gji/ggx009.

Ryan, W. B. F., S. M. Carbotte, J. O. Coplan, S. O'Hara, A. Melkonian, R. Arko, R. A. Weissel, V. Ferrini, A. Goodwillie, F. Nitsche, J. Bonczkowski, and R. Zemsky (2009), Global multi-resolution topography synthesis, *Geochemistry, Geophysics, Geosystems*, *10*(3), doi: 10.1029/2008gc002332.

Schmalzle, G. M., R. McCaffrey, and K. C. Creager (2014), Central cascadia subduction zone creep, *Geochemistry, Geophysics, Geosystems*, *15*(4), 1515–1532, doi: 10.1002/2013GC005172.

Shackleton, N. J. (1987), Oxygen isotopes, ice volume and sea level, *Quaternary science reviews*, *6*(3), 183–190, doi: 10.1016/0277-3791(87)90003-5.

Shennan, I., S. Bradley, G. Milne, A. Brooks, S. Bassett, and S. Hamilton (2006), Relative sea-level changes, glacial isostatic modelling and ice-sheet reconstructions from the british isles since the last glacial maximum, *Journal of Quaternary Science*, *21*(6), 585–599, doi: 10.1002/jqs.1049.

Shugar, D. H., I. J. Walker, O. B. Lian, J. B. R. Eamer, C. Neudorf, D. McLaren, and D. Fedje (2014), Post-glacial sea-level change along the pacific coast of north america, *Quaternary science reviews*, *97*, 170–192, doi: 10.1016/j.quascirev.2014.05.022.

Stammer, D., A. Cazenave, R. M. Ponte, and M. E. Tamisiea (2013), Causes for contemporary regional sea level changes, *Annual review of marine science*, *5*, 21–46, doi: 10.1146/annurev-marine-121211-172406.

Stouthamer, E., and S. van Asselen (2015), Potential of holocene deltaic sequences for subsidence due to peat compaction, in *Proceedings of IAHS*, vol. 372, pp. 173–178, Copernicus GmbH, doi: 10.5194/piahs-372-173-2015.

United States. Federal Geodetic Control Committee (1984), *Standards and Specifications for Geodetic Control Networks*, National Geodetic Information Branch, NOAA, FGCC.

Verdonck, D. (2006), Contemporary vertical crustal deformation in cascadia, *Tectonophysics*, *417*(3), 221–230, doi: 10.1016/j.tecto.2006.01.006.

Wang, K., and A. M. Tréhu (2016), Invited review paper: Some outstanding issues in the study of great megathrust earthquakes—the cascadia example, *Journal of Geodynamics*, *98*, 1–18, doi: 10.1016/j.jog.2016.03.010.

Wang, K., J. He, H. Dragert, and T. S. James (2001), Three-dimensional viscoelastic interseismic deformation model for the cascadia subduction zone, *Earth, Planets and Space*, *53*(4), 295–306, doi: 10.1186/BF03352386.

Wang, K., R. Wells, S. Mazzotti, R. D. Hyndman, and T. Sagiya (2003), A revised dislocation model of interseismic deformation of the cascadia subduction zone, *Journal of geophysical research*, *108*(B1), doi: 10.1029/2001jb001227.

Williams, T., and R. C. McPherson (2006), Gorda plate deformation contributes to shortening between the klamath block and the on-land portion of the accretionary prism to the s. cascadia subduction zone, in *Friends of the Pleistocene Field Trip Guidebook, The Triangle of Doom: Signatures of Quaternary Crustal Deformation in the Mendocino Deformation Zone (MDZ) Arcata, CA*, edited by M. Hemphill-Haley, R. McPherson, J. R. Patton, J. Stallman, T. H. Leroy, D. Sutherland, and T. B. Williams, pp. 102–110.

Williams, T. B., H. M. Kelsey, and J. T. Freymueller (2006), GPS-derived strain in northwestern california: Termination of the san andreas fault system and convergence of the sierra Nevada–Great valley block contribute to southern cascadia forearc contraction, *Tectonophysics*, *413*(3-4), 171–184.

Wilson, D. S. (2002), The juan de fuca plate and slab: Isochron structure and cenozoic plate motions, *Tech. rep.*, USGS.

Zervas, C., S. Gill, and W. Sweet (2013), Estimating vertical land motion from long-term tide gauge records, *Tech. rep.*, NOAA, doi: 10.25607/OBP-141.

Zervas, E. C. (2009), Sea level variations of the united states, 1854-2006, *Tech. Rep. NOS CO-OPS 053*, NOAA.